JOM
https://doi.org/10.1007/s11837-019-03614-5

Effect of Interface Structure on the Hydrophobicity, Mechanical and Optical Properties of HfO_2/Mo/HfO_2 Multilayer Films

P. DUBEY,[1] ANIL K. BATTU,[1,2,3] V. SHUTTHANANDAN,[2,3] and C.V. RAMANA[1,2,4]

1.—Department of Mechanical Engineering, University of Texas at El Paso, El Paso, TX 79968, USA. 2.—Center for Advanced Materials Research (CMR), University of Texas at El Paso, El Paso, TX 79968, USA. 3.—Environmental Molecular Sciences Laboratory, Pacific Northwest National Laboratory, Richland, WA 99352, USA. 4.—e-mail: rvchintalapalle@utep.edu

We report on the super-hydrophobicity and tunable and optical and mechanical properties of transparent HfO_2(50 nm)/Mo(20 nm)/HfO_2(50 nm) multilayer films facilitated by engineering the ceramic–metal interface microstructure. A comparative study of nano-columnar and glassy (dense) structured HfO_2/Mo/HfO_2 multilayer films demonstrate the remarkable effect of interface structure on their hydrophobicity and mechanical properties. The nano-columnar structured multilayer films exhibit the dominance over the glassy structured stack in terms of their enhanced characteristics, namely the mechanical characteristics, anti-reflection behavior, visible transmittance, and hydrophobicity. While hydrophobicity is derived from the combined effect of hierarchical surface roughness and nano-columnar structure of the top and bottom Hf-oxide ceramic layers, the enhanced mechanical response is derived from the columnar structure of Mo metallic interlayer vertically aligned with overall multilayer stack. The combination of super-hydrophobicity and enhanced mechanical properties of optically transparent HfO_2/Mo/HfO_2 multilayer films through HfO_2–Mo interface structure control as demonstrated in this work may provide a pathway to further tune the efficiency and in the optimization of architectures for energy-saving applications.

INTRODUCTION

Engineering the surface and interface structure at nanoscale dimensions has emerged as one of the best tools to unlock the full potential of advanced materials in energy production, conversion and related technologies.[1–5] Especially, for energy-saving architectures, the surface/interface microstructure in dielectric(D)/metal(M)/dielectric(D) multilayered films, where the component layers face stringent requirements, is critical to tailor the performance.[6,7] The fundamental requirement of a D/M/D, where D is usually an oxide ceramic in combination with a suitable metal M, is the ability to transmit nearly all of the energy in the visible (i.e., high-transparency) region and reflect a part or all the energy in the infrared (i.e., cooling) region of the electromagnetic spectrum.[3,4,7] When used in windows and panels, the energy delivered to buildings could be saved by properly modifying and/or controlling the solar transmission into the building using efficient glass technologies with the same, or higher, levels of comfort and expediency. The general architecture and functionality of each component layer in the D/M/D multilayer configuration is shown in Fig. 1. The initial D layer, in addition to protecting the M layer from environmental effects, serves as a low absorbing anti-visible reflection coating to improve visibility via destructive interference of the reflected visible light. The M layer acts as an infrared absorber or reflector. The final D layer contributes to the destructive interference of the reflected visible light as well as providing a nucleation support to the M interlayer.[4,7–10] Tuning physical and electronic properties of D/M/D multilayer films is the most efficient method to enable solar spectral control and enhanced energy-saving performance. However, while focus toward the mechanical and thermo-chemical durability of such multilayered film configuration is meager, the

Published online: 25 June 2019

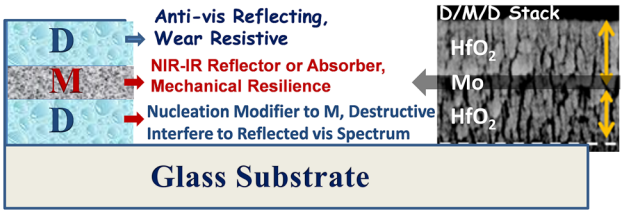

Fig. 1. Functionality of each layer in D/M/D multilayer film architecture.

mechanical properties of D/M/D are also of paramount importance from the point of view of practical applications. The obvious reason is that, as thin coatings on windows, etc., multilayer films must survive harsh or even unexpected environmental/climate conditions. Mechanical durability protects the D/M/D-coated windows from environment impacts and abrasion from the dust particles and hailstorms. Therefore, tuning the mechanical properties along with the optical constants of D/M/D films to meet the requirements of a given technological application is critical. While material selection and electronic properties allow the obtaining of the desired spectral properties, we demonstrate that the controlled mechanical properties can be achieved by engineering the interfaces and structure of the component ceramic and metal layers at the nanoscale. Furthermore, these D/M/D films are often produced by physical vapor deposition methods, in which optimizing the processing conditions allow the fabrication of component layers with controlled microstructures.[7,11–16] In this context, by investigating the structure–property relationship in HfO_2/Mo/HfO_2 multilayer films, the remarkable effect of controlled, component-layer-mediated nano-columnar structures with hierarchical surface roughness to significantly improve their hydrophobicity and mechanical properties is demonstrated.

For D/M/D layers, high dielectric constant (> 20) films with the same thickness for the top and bottom D-layers sandwiched together with a mechanically resilient metal (M) in between are common.[4,17] HfO_2, an important oxide dielectric, is an attractive choice for D/M/D in addition to serving a wide range of other technological applications.[18–25] HfO_2 possesses a high dielectric constant (~ 25), large band gap (5.6 eV), high refractive index (2.1) and good thermo-mechanical properties.[18–25] For the M interlayer, Mo is an ideal candidate.[26–31] In addition to having a mechanically resilient nature, Mo films exhibit the desired reflectance (low in visible, high in infrared), optimum conductivity, and slow heterogeneous electron transfer kinetics.[26–31] Demkov reported that the presence of Mo allows the formation of extended Frankel pairs with a formation energy of only 1.4 eV,[32] leading to O-vacancies on the HfO_2 side of the interface, which modifies the effective work function of the Mo. The structural and optical properties of D/M/D films with HfO_2 as a dielectric in combination with different metals have been reported in the literature.[33–36] Specifically, it is important to note that D/M/D multilayer films have been used for heat mirror applications, where the HfO_2 dielectric was used in conjunction with Mo, Al and Ag.[20,33–36] Heat mirrors fabricated using HfO_2 and Ag (i.e., HfO_2/Ag/HfO_2) in D/M/D multilayer films showed an average transmittance of 72% and an average reflectance of 67% in the NIR region (700–2000 nm).[34] Selvakumar et al. have studied heat mirrors with HfO_2/M/HfO_2 (M = Hf, Mo, Al) multilayer films fabricated by magnetron sputtering.[3,35] A high solar absorptance of 90.5–92.3% was reported for HfO_2/Mo/HfO_2 and 91.6–92.5% for HfO_2/Hf or Al/HfO_2 heat mirrors.[3,35] However, while significant attention has been directed towards the spectral characteristics, a detailed understanding of the effect of interface structure and morphology on the hydrophobicity and mechanical response of HfO_2/Mo/HfO_2 multilayer films is lacking at this time. The present work was performed to fill this knowledge gap.

EXPERIMENTAL DETAILS

Fabrication of HfO_2/Mo/HfO_2 Multilayered Films

Multilayer films of HfO_2/Mo/HfO_2 were deposited on Si(100) and Corning glass substrates via electron beam evaporation and magnetron sputtering. HfO_2 and Mo pellets from Plasmaterials were used as the evaporation materials. Before placing into respective vacuum chambers, all the substrates were cleaned and dried with nitrogen and then placed on the substrate holder. The e-beam and magnetron sputtering deposition parameters are presented in Table I.

For the electron beam deposition, the D/M/D multilayer films were deposited in a sequence of 50 nm, 20 nm, and 50 nm for HfO_2, molybdenum (Mo), and HfO_2, respectively. The sample has been designated as $S4_E$. The multilayers were deposited in situ from a copper multi-hearths system without exposing the samples to ambient pressure during deposition material changes. A thermocouple, provided close to the substrate holder, measured the temperature during deposition, while the sample thickness was monitored using a quartz thickness monitor. At the initiation of evaporation, the difference is set as “zero” thickness and the system is calibrated by selecting the material to be deposited. Moreover, the evaporation rate is further refined/cross-verified by measuring the cross-sectional thickness of the test films using secondary electron microscopy.

RF/DC magnetron-sputtered multilayer films, designated as $S4_M$, were deposited from 2-inch-diameter (c.50 mm) hafnium (Hf) and molybdenum (Mo) targets (Plasmaterials) and followed the same deposition order and thickness values as the electron beam-deposited samples. In situ deposition of HfO_2 layers and the Mo layer were performed to

Table I. E-beam evaporation and magnetron sputtering deposition parameters employed for the fabrication of HfO_2/Mo/HfO_2 multilayer films

Deposition parameters	E-beam evaporation	Magnetron sputtering
Targets/pellets	Hafnium oxide (HfO_2, 99% purity) and Molybdenum (Mo, 99.95% purity)	Hafnium (Hf, 99. 95% purity) and Molybdenum (Mo, 99. 95% purity)
Gas used	No	Hf: Ar (28 sccm) + O_2 (12 sccm) Mo: Ar (40 sccm)
Residual pressure	8×10^{-7} Torr	$\sim 1 \times 10^{-7}$ Torr
Deposition pressure	HfO_2, Mo: 4×10^{-6} Torr	HfO_2, Mo: 15×10^{-3} Torr
Deposition rate	HfO_2: $\sim$ 1 Å/s Mo: $\sim$ 0.3 Å/s	HfO_2: $\sim$ 0.2 Å/s Mo: $\sim$ 0.7 Å/s
Power targets	HfO_2, Mo: current 150 mA, and Filament voltage $\sim$ 8.15 kV	Hf: 100 W RF Mo: 40 W DC
Substrate target distance	$\sim$ 180 cm	6 cm
Substrate temperature	25–40°C	25°C

avoid surface contamination. To remove residual oxygen from the chamber after the deposition of the bottom HfO_2 layer, the sputtering chamber was evacuated again up to 8×10^{-7} Torr.

Characterization

Crystal Structure and Phase Analysis

Grazing incidence x-ray diffraction (GIXRD) was used for phase analysis of the $S4_E$ and $S4_M$ multilayer films. A Bruker D8 Advance diffractometer was employed for the GIXRD measurements with Cu-K_α radiation (λ = 1.54 Å) x-ray. Diffraction measurements were carried out on a detector scan mode in the range of 15°–60° with a step size and scan speed of 0.02° and 1 s/step, respectively.

Microstructure and Morphology Measurements

An ultra-high-resolution scanning electron microscope (SEM; Hitachi S-4800) was used for surface imaging analysis of the samples. Additionally, cross-sectional SEM imaging was performed on the $S4_E$ and $S4_M$ multilayer films deposited on the Si samples using a $\sim$ 3-nm-thick gold coating and carbon paste at the ends of samples to avoid charging problems. The surface roughness of the D/M/D multilayer films by the root mean square (rms) process was evaluated using a scanning probe microscope (SPM; Hysitron TI750).

Chemical Composition

Elemental composition analysis and depth profiling were carried out using energy dispersive x-ray spectroscopy (EDS; Oxford), X-Max, and x-ray photoelectron spectroscopy (XPS; Kratos Analytical, Manchester, UK) in order to confirm the integrity of the layered structure, in addition to evaluating the depth distribution of the single layers. For the XPS depth profiling, the samples were sputtered using 5 keV Ar + ion beams raster over a 2×2 mm^2 area of the sample, and survey scans were typically carried out at pass energies of 80 or 160 eV.

Contact Angle Measurements

A constant volume sessile drop method was used to measure the contact angle values. The wettability of the multilayer film was measured using a contact angle meter (ramé-hart Model 250 Standard Goniometer/Tensiometer) immediately after the deposition process to avoid surface contamination. The contact angles reported are the average values of ten different measurements taken on films obtained with a drop of $\sim$ 8 μL in volume.

Mechanical Characteristics

Mechanical properties, hardness (H) and reduced elastic modulus (E_r), of deposited DMD films were obtained through nanoindentation tests carried out on a Hysitron T1750 Tribo nanoindentor. The nanoindentation measurements were performed using a triangular pyramid Berkovich diamond indenter with a normal angle of 65.3° between the tip axis and the faces of the triangular pyramid, and an effective size of the apex of approximately 100 nm. A commonly accepted rule suggests that the substrate measurements can be obtained if the indentation depth is kept to less than 10% of the film thickness. At such small indentation loads, the resulting indents on the thin films can be microscopic to submicroscopic in size. Therefore, measuring these small indents is very difficult and generally accurate. Thus, the most commonly utilized method is to gauge the size of the indentation

from the loading and unloading curves generated during the test. The deformation during loading is assumed to possess elastic/plastic tendency, whereas, during unloading, it is assumed that only elastic displacements are recovered which is the elastic nature of the unloading curve that facilitates analysis. Therefore, the standard procedure was employed to derive the mechanical properties with the help of loading and unloading curves. The Oliver and Pharr method[12] was employed to calculate the mechanical characteristics (H and E_r). With this approach, E_r can be calculated by finding the stiffness (S) of the film from the slope of the unloading curve. The relationship between E_r and S can be described using:

$$E_r = \frac{\sqrt{\pi}}{2}\frac{S}{\sqrt{A}} \quad (1)$$

where A is defined as the area of contact at peak load. To find the hardness value, the same value for the area of contact is used along with the maximum load (P_{max}) in:

$$H = \frac{P_{max}}{A} \quad (2)$$

To minimize the substrate effect, the load-controlled indentation tests were initially performed on each sample to determine the maximum depth that would not be more than 10% of the total film thickness. Seventeen indents of the selected 200 μN load were performed at 0.2 s^{-1} strain rate, and the average H and E_r values were calculated for each sample.

RESULTS AND DISCUSSION

Crystal Structure and Phase

The GIXRD patterns of the HfO_2(50 nm)/Mo(20 nm)/HfO_2(50 nm) multilayer films are shown in Fig. 2. The HfO_2/Mo/HfO_2 multilayer films, fabricated by electron beam evaporation and sputter-deposition, are designated as $S4_E$ and $S4_M$, respectively. It is evident (Fig. 2a) that the GIXRD pattern for sample $S4_M$ exhibits the presence of diffraction peaks indicating the polycrystalline nature of the samples. However, the GIXRD patterns of $S4_E$ exhibits a broad and diffuse pattern indicating the characteristic amorphous nature. GIXRD peak indexing, as shown in Fig. 2, indicates the presence of monoclinic (m) HfO_2 and cubic (c) Mo in the D/M/D samples made by sputter-deposition ($S4_M$). It has been reported in the literature that magnetron-sputtered HfO_2 films on non-metal and crystalline metal substrates are amorphous and polycrystalline, respectively.[3,20,37–40] Hence, the GIXRD data of $S4_M$ suggest that the presence of crystalline Mo films, as an interlayer, promotes the crystalline growth of HfO_2 (top D) film. To make this point clear, the GIXRD pattern of the bottom-HfO_2 films is shown in Fig. 2b. It can be seen that the data

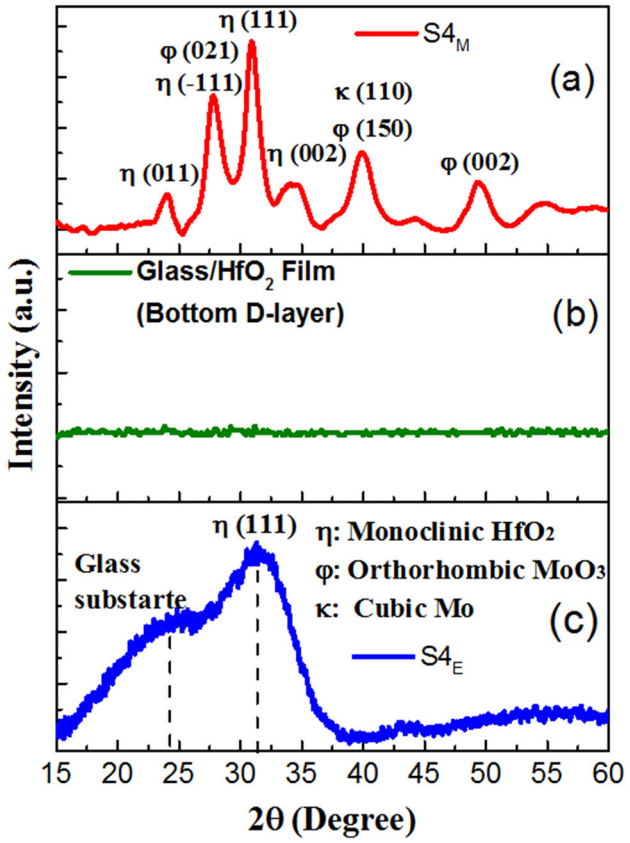

Fig. 2. GIXRD patterns of the HfO_2/Mo/HfO_2 multilayer films: (a) $S4_M$; (b) HfO_2 film; and (c) $S4_E$. The structural differences are evident from the comparison of the data.

exhibit a diffuse nature of the pattern without any indication of the peaks. Thus, it is evident that the underlying HfO_2 films (bottom D layer) are amorphous. The data (Fig. 2b) in comparison with the data of entire D/M/D multilayer films also highlight the effect of the Mo interlayer in promoting the polycrystalline nature of the top-HfO_2 films. This observation of the polycrystalline nature of the HfO_2 layer in the D/M/D configuration is consistent with the literature.[3,4,33–36] It has been demonstrated that the amorphous nature and/or crystallization of the D/M/D multilayer films is influenced by the microstructure and chemical purity of the M interlayer.[3,4,33–36] For the HfO_2 dielectric, the presence of a metallic interlayer promotes crystallization.[3,4,33–36] However, the Al interlayer deteriorates the crystalline nature of the HfO_2/Al/HfO_2 which is attributed to the induced stress due to the mismatch and ionic size difference of Al and Hf.[33]

The GIXRD pattern of $S4_E$ is shown in Fig. 2c, in which a characteristic amorphous hump corresponding to the glass substrate can be seen. The other hump at $\sim 32°$ can be attributed to the (111) peak of m-HfO_2.[34] The estimated crystallite size is ~ 1.5 nm corresponding to the (111) peak of m-HfO_2. The crystallite size is calculated from

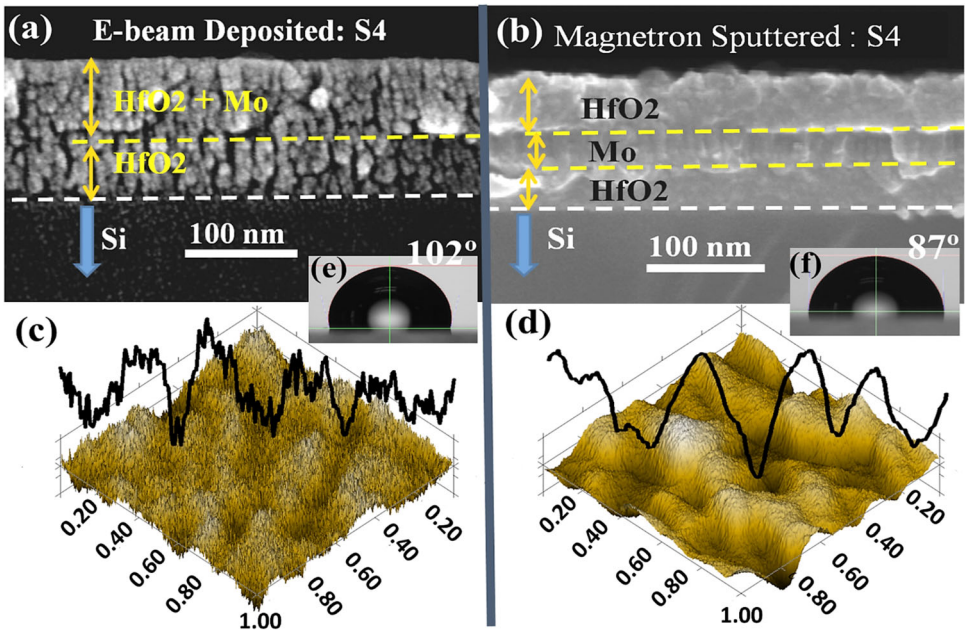

Fig. 3. (a) Cross-sectional SEM image of $S4_E$ multilayer film (inset contact angle values), (b) cross-sectional SEM image of $S4_M$ multilayer film (inset contact angle values), (c) topographical SPM micrograph of $S4_E$ multilayer film with line profile curve, and (d) topographical SPM micrograph of $S4_M$ multilayer film with line profile curve.

Scherrer's formula.[19] Note that the amorphous nature has been reported widely in the literature for HfO_2 film deposited at room temperature.[37–40] The GIXRD peaks indexed to *c*-Mo for $S4_M$ were not observed for $S4_E$. This might be attributed to either very low peak intensities of the e-beam-evaporated Mo layer overlapped with background noise data or might be in the amorphous state.

Chemical Composition and Elemental Analysis

The atomic concentration (at.%) of O, Mo, and Hf in $HfO_2/Mo/HfO_2$ films has been obtained using EDS. While it was extremely difficult to determine the composition of individual layers, the composition is estimated over the depth of the entire D/M/D multilayer stack. The atomic concentration of O, Hf and Mo in $S4_M$ are 66%, 33% and balanced Mo, respectively. The measurements were made at six different locations on the surface. The EDS results agree well with the expected stoichiometry. Note that the deposition and characterization of sputter-deposited Mo and Hf oxide films have previously been extensively discussed by our team.[36–41] Thus, in view of the high confidence level of elemental composition of the sputtered ($S4_M$) samples, the x-ray photoelectron spectroscopic analysis has been performed on the electron beam-evaporated ($S4_E$) multilayer films. Specifically, XPS depth profiling was employed, in addition to EDS, to determine the chemical state and composition. XPS depth profiling also confirm the integrity of the depth distribution of the component layers. The data indicate that the top layer has Hf $\sim$ 33.3 at.% and O $\sim$ 66.7 at.% maintaining the HfO_2 stoichiometry as expected.[36] Furthermore, the interface chemical quality and respective layer composition is well maintained in the $HfO_2/Mo/HfO_2$ films. Thus, the XPS data confirm the stoichiometry and chemical integrity.

Surface and Interface Microstructure

The SEM micrographs of the surface and interface structure of the $S4_E$ and $S4_M$ multilayer films are presented in Fig. 3. A marked difference is seen in the structure and morphology (Fig. 3) of the $S4_E$ and $S4_M$ multilayer films. A characteristic columnar growth pattern of $S4_E$ multilayer film is evident in Fig. 3a. The relatively large thickness of the top layer and the growth pattern in comparison to the bottom layer indicate the columnar growth of the Mo interlayer over the bottom HfO_2 layer. This has been confirmed by the XPS results that the $\sim$ 20-nm-thick Mo interlayer is sandwiched between equally thick ($\sim$ 50 nm) HfO_2 layers.[36] This implies that the bottom HfO_2 columns act as nucleation sites for the Mo interlayer. Therefore, the multilayer films in micrograph appear with a $\sim$ 50-nm-thick first layer and a $\sim$ 65-nm-thick second layer with different columnar gaps. Moreover, the effect of the Mo interlayer can be seen in the morphology, where the effect is predominantly in the growth and columnar size of the multilayer films. The first layer exhibits large inter-columnar spacing as compared to the second layer, which exhibits narrow inter-columnar spacing. Statistical data analysis of the image (Fig. 3a), as performed by Image J 1.48 V

software, indicates columnar grains of 10–22 nm of width and ~ 50 nm in length with 3–8 nm of inter-columnar spacing in the first layer. However, the second layer is relatively compact with a fine columnar size of ~ 5–16 nm in width and ~ 60–75 nm in length and narrower (~ 0.5–3 nm) inter-columnar spacing. The observed columnar structure may be the consequence of low atomic mobility and the shadowing effects during e-beam deposition. Moreover, the slow heterogeneous electron transfer kinetics of the Mo atoms during deposition supports the nucleation of the Mo interlayer with a sufficiently high linear density along step edges of bottom the columnar HfO_2 layer.[27] On the other hand, $S4_M$ clearly reveals the non-columnar dense structure of the top and bottom HfO_2 layers sandwiching a dense structured Mo interlayer. The topographical micrographs with line profile graphs of $S4_E$ and $S4_M$ multilayer films are shown in Fig. 3c and d, respectively. A triangular pyramid Berkovich diamond has been used to scan the 1 × 1 μm^2 area of the films. The surface roughness as measured in rms values of $S4_E$ (~ 1 nm) and $S4_M$ (~ 4 nm) indicate that the dense structured multilayer film ($S4_M$) is relatively rough compared to the nano-columnar structured multilayer film ($S4_E$). However, the line profile graphs infer that the $S4_E$ film exhibits a high hierarchical (multiscale) surface roughness[42,43] over $S4_M$. For quantification of the hierarchical roughness values, the total number of changes in the sign of the gradient (positive to negative or conversely) at the consecutive points along the line profile has been calculated.[42,43] It is observed that the number of such changes in $S4_E$ are higher (152) compared to $S4_M$ (58). The nanocrystalline phase and columnar structure with fine inter-columnar space in the $S4_E$ (Figs. 2 and 3) may be the reason for the observed high hierarchical roughness. Most important to note is the fact that the effect of hierarchical roughness is significant on the contact angle, as shown in the inset of Fig. 3. We believe that the hydrophobicity, which is quite useful for designing energy-saving windows, is primarily derived from the HfO_2 top(D)-layer, in which the reported contact angle values are ~ 74°–90°.[19,20] Traditionally, the structure of HfO_2 with higher surface roughness attains the higher contact angle.[19,20] However, in the present case of HfO_2/Mo/HfO_2 multilayer films, the contact angle of $S4_E$ is higher (102°) compared to that (87°) of $S4_M$. Such a large difference in contact angle can only be accounted for on the basis of difference sin surface morphologies and structures of the $S4_E$ and $S4_M$ multilayer films. Note that the surface rough of $S4_E$ is lower compared to that of $S4_M$. However, $S4_E$ is characterized by the higher hierarchical surface roughness coupled with well-aligned interfacial nano-columnar structure which are not seen in $S4_M$. Thus, the higher contact angle (102°) of nano-columnar structured $S4_E$ with lower surface roughness value (~ 1 nm) over polycrystalline, relatively dense $S4_M$ with higher surface roughness (~ 4 nm), is believed to be due to the dominating hierarchical surface roughness value of $S4_E$.

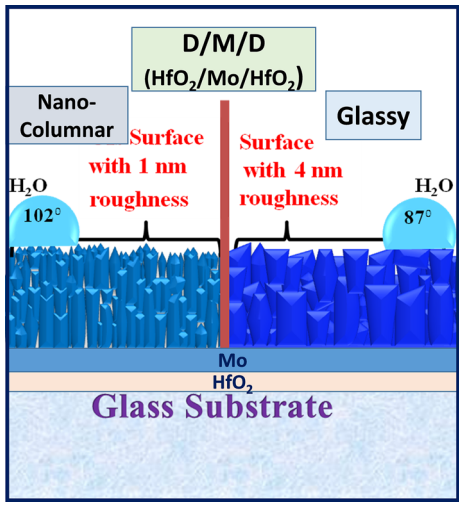

Fig. 4. Model representing the effect of hierarchical surface roughness on the contact angle value of nano-columnar structured ($S4_E$) and dense structured ($S4_M$) HfO_2(50 nm)/M(20 nm)/HfO_2(50 nm) multilayer films.

A model representing the effect of nano-columnar and nanocrystalline structure-induced hierarchical surface roughness on the contact angle value of nano-columnar structured ($S4_E$) and dense structured ($S4_M$) HfO_2(50 nm)/M(20 nm)/HfO_2(50 nm) films is shown in Fig. 4. The high hierarchical roughness value of $S4_E$ enhances the surface interaction with air by creating multiple composite interfaces (CIs) with air pockets in the valleys between asperities. The assumption is that the liquid may not fill the surface cavities, creating air pockets. Hence, such CIs dramatically decrease the solid–liquid contact area and significantly increase the contact angle, resulting in very high hydrophobic nature of $S4_E$ while $S4_M$ is hydrophilic, despite the fact that it has a polycrystalline surface of higher rms roughness. Such hierarchical roughness or CIs was found to be an important factor to achieve super-hydrophobic nature in natural and artificial surfaces.[44,45] The hierarchical roughness is also an important parameter for the development of optical coatings for the utilization in the ultraviolet region and directed energy in near infrared (NIR) to infrared (IR) reflecting heat mirrors.[43–46]

Mechanical Properties

For practical applications of D/M/D multilayer films, either in energy efficient windows or transparent/heat-managing layers, the mechanical properties are also important. The mechanical properties, namely the hardness (H) and reduced elastic modulus (E_r), of the D/M/D multilayer films are presented in Fig. 5. The depth of penetration of the indenter into the surface, at a 200 μN load is shown in the inset (Fig. 5). The results indicate that

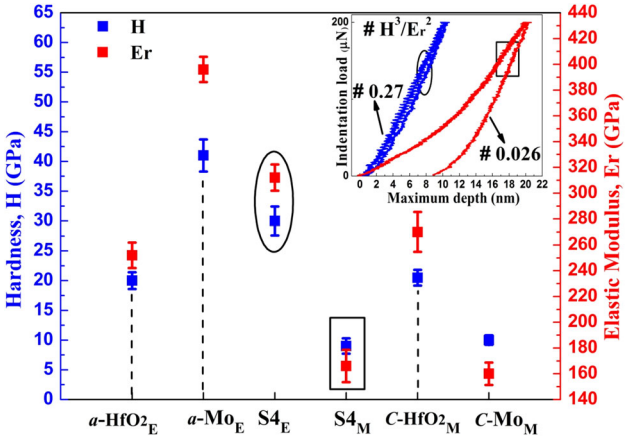

Fig. 5. Hardness and reduced elastic modulus of the $S4_E$ and $S4_M$ multilayer films (inset loading and unloading graphs of $S4_E$ and $S4_M$).

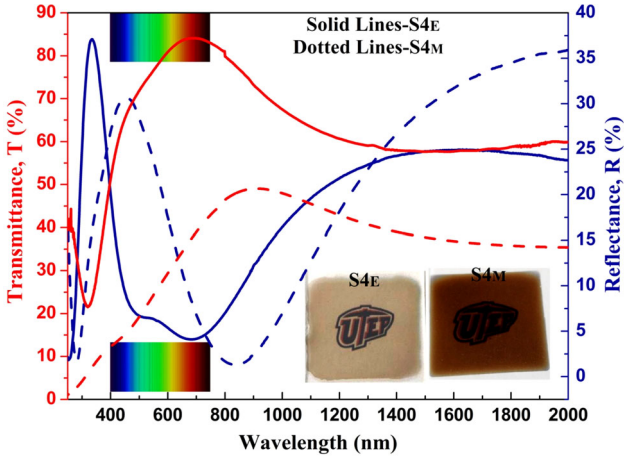

Fig. 6. Spectral transmittance and reflectance characteristics of HfO_2/Mo/HfO_2 multilayer films.

$S4_E$ exhibits significantly higher values compared to $S4_M$. The mechanical parameters for $S4_E$ are H = 30 GPa, E_r = 312 GPa compared to H = 9 GPa, E_r = 166 GPa for $S4_M$. The columnar structure with inter-columnar spacing, as discussed in the model (Fig. 4), makes it more difficult for dislocations to link together and propagate during load application. The interlocking of dislocations is attributed to the observed higher H of $S4_E$. Moreover, the spacing between columns absorbs compressive deformation; therefore, the columnar structure is able to accommodate more compressive deformation during indentation.[42,44]

The loading–unloading profiles reveal that the indenter penetrates 8% less in $S4_E$ than in $S4_M$. Additionally, the plastic coercivity of the graphs that can be estimated quantitatively by calculating the H^3/E_r^2 value infers that the $S4_E$ film (H^3/E_r^2 = 0.28) resists the plastic deformation 10 times better than $S4_M$ (H^3/E_r^2 = 0.026).[47] The mechanical properties (H and E_r) of individual D (HfO_2) and M (Mo) films are also presented in Fig. 5 for comparison. The experimentally determined H and E_r values are presented for (1) EB-deposited amorphous HfO_2 film (~ 100 nm); (2) amorphous Mo film (~ 100 nm); (3) magnetron sputtered polycrystalline HfO_2 film (~ 100 nm); and (4) polycrystalline Mo film (128 nm). Comparison of the data indicates the significant role of the structure of the Mo interlayer to control the H and E_r of the multilayer HfO_2/Mo/HfO_2 films. Moreover, the Mo interlayer also affects the evolution of the structure of the top HfO_2. Furthermore, an increase in crystallization of the top HfO_2 (D) layer with increasing Mo thickness in HfO_2/Mo/HfO_2 has been observed (not shown). Hence, a combination of nanocrystalline nano-columnar structure of both the Mo metallic interlayer and the HfO_2 layers significantly enhances the mechanical response of D/M/D multilayer films.[47] The combination of hydrophobicity and mechanical durability is rarely found in nature due to the inconclusiveness of hydrophobicity after mechanical wear.[48] It has been reported in the literature that superhydrophobic surfaces with high contact angles exhibit a self-cleaning effect and low drag for fluid flow.[48] The abrasive wear of the surface may lose the hydrophobic nature of the surface; hence, the enhanced mechanical properties (H ~ 25–30 GPa, E_r ~ 300–400 GPa and $H^3/E_r^2 > 0.1$ GPa) make the surface resistant to abrasive wear and preserve the hydrophobicity of the surface.

Optical Properties

The spectral transmittance (T) and reflectance (R) of $S4_E$ and $S4_M$ multilayer films are presented in Fig. 6. Almost a similar trend in spectral transmittance along with maximum T% in the visible (~ 630–770 nm) range for $S4_E$ multilayer film and in the NIR (~ 820–860 nm) for the $S4_M$ multilayer film can be noted. Moreover, the nano-columnar structure of the D/M/D multilayer film is beneficial in increasing the T% in the visible range. The average T% in the visible region for $S4_E$ is ~ 76%, whereas that of $S4_M$ is only 30%. Furthermore, $S4_E$ (nano-columnar structure) displays only ~ 6% average reflectance in the visible region, while that of $S4_M$ (dense structure) is ~ 20%. A very weak visible reflectance, ~ 3% at ~ 650 nm, of the $S4_E$ multilayer film strongly supports its ability to serve as an anti-reflection coating in the visible range of wavelengths.[44] This anti-reflection feature might originate from the nano-columnar morphology of layers with tuned refractive index values. On the other hand, both $S4_E$ and $S4_M$ exhibit almost similar (~ 25%) reflectance in the IR region. The other significant effect of the nano-columnar structure with high hierarchical roughness over the glassy structure can be seen in the ultraviolet spectral region. The nano-columnar structure reflects 10% more compared to the dense structure. It is believed that the nano-columnar structure with zigzag CIs (hierarchical roughness) plays an important role in increasing the T% and lowering the R% in the

visible region. The cross-sectional and topographical micrographs (Fig. 4) also support these findings in the difference in their optical behavior. The inset of Fig. 6 shows the topographical optical appearance of the nano-columnar structured ($S4_E$) and dense structured HfO_2/Mo/HfO_2 multilayer films deposited on glass substrates. The coated glass substrates were placed on top of the UTEP logo. A high visibility of the UTEP logo can be seen clearly in the $S4_E$ multilayer film as compare to the $S4_M$ multilayer film. These observations indicate that the interface microstructure tuning may allow better control or tailoring of the electronic properties. While the interface microstructure influence on the optical properties is evident, a direct comparison of the optical properties of the HfO_2/Mo/HfO_2 multilayer films in this work with those reported in the literature may not be meaningful since the thickness values of the D and M layers, and their respective configurations, are different. However, we present a comparison of the present data with those of the D/M/D multilayer films containing HfO_2 as a dielectric in combination with different metals.[3,20,33,35] Specifically, it is imperative to compare and contrast the results with some of the existing reports on D/M/D multilayer films for heat mirror applications, where the HfO_2 dielectric was used in conjunction with Mo, Al and Ag.[3,20,33,35] Heat mirrors, fabricated using HfO_2 and Ag (i.e., HfO_2/Ag/HfO_2) in D/M/D multilayer films, showed an average transmittance of 72% and an average reflectance of 67% in the NIR region (700–2000 nm).[20] Selvakumar et al. have studied heat mirrors with HfO_2/M/HfO_2 (M = Hf, Mo, Al) multilayer films fabricated by magnetron sputtering.[3,35] A high solar absorptance of 90.5–92.3% was reported for HfO_2/Mo/HfO_2 and 91.6–92.5% for HfO_2/Hf or Al/HfO_2 heat mirrors. While the spectral transmittance of HfO_2/Mo/HfO_2 multilayer films in this case are comparable to these existing studies, their IR blocking efficiency is still low. This could be due to the fact that we considered one specific example of a selected thickness configuration of HfO_2/Mo/HfO_2 films, where the focus was to demonstrate the effect of interface microstructure. However, the results presented in this work warrant further consideration to optimize the microstructure and optimal thickness values so that the best possible efficiencies can be achieved.

CONCLUSION

A detailed, comparative study of the hydrophobicity and mechanical durability of nano-columnar structured and dense structured HfO_2/Mo/HfO_2 multilayered films is presented. The results demonstrate the significant effect of interfacial structure evolution on the hydrophobicity and mechanical properties of HfO_2/Mo/HfO_2 multilayer films. A nanocrystalline (surface), nano-columnar (interface) structure with vertical alignment through the dielectric and metal interface enhances the overall hierarchical surface roughness, which in turn improves the hydrophobic nature and mechanical stability. The combination of hydrophobicity ($\theta > 100°$) and enhanced mechanical properties ($H \sim 25$–30 GPa, $E_r \sim 300$–400 GPa, $H^3/E_r^2 > 0.1$ GPa), achieved through structure control in this work, may be beneficial to further optimize the efficiency of D/M/D multilayer films for energy-saving applications. Specifically, these findings provide evidence that interface engineering and control of the structure, across the surfaces/interfaces in multilayered films, can significantly improve the hydrophobicity and mechanical durability, which are desired to realize efficient solar selectivity for energy saving in practical device applications.

ACKNOWLEDGEMENTS

The authors acknowledge, with pleasure, support from the National Science Foundation (NSF) with Grant #ECCS-1509653. One of us (C.V.R.) also acknowledges the NSF support with Grant #DMR-1827745. A portion of some work has been carried out in the Environmental Molecular Sciences Laboratory (EMSL), a National Scientific User Facility located at the Pacific Northwest National Laboratory (PNNL) and supported by the U.S. DOE Office of Biological and Environmental Research. PNNL is operated by Battelle Memorial Institute for the U.S.DOE under Contract DE-AC 06-76RLO 1830.

REFERENCES

1. B.A. Kemp, *Nat. Photonics* 10, 291 (2016).
2. M.A. Basyooni, M. Shaban, and A.M. El Sayed, *Sci. Rep.* 7, 41716 (2017).
3. N. Selvakumar, H.C. Barshilia, K.S. Rajam, and A. Biswas, *Sol. Energy Mater. Sol. Cells* 94, 1412 (2010).
4. M.F. Al-Kuhaili, A.H. Al-Aswad, S.M.A. Durrani, and I.A. Bakhtiari, *Sol. Energy* 86, 3183 (2012).
5. J.H. Kim, H.-K. Lee, J.-Y. Na, S.-K. Kim, Y.-Z. Yoo, and T.-Y. Seong, *Ceram. Int.* 41, 8059 (2015).
6. J.H. Kim, Y.-J. Moon, S.-K. Kim, Y.-Z. Yoo, and T.-Y. Seong, *Ceram. Int.* 41, 14805 (2015).
7. A.M. Al-Shukri, *Desalination* 209, 290 (2007).
8. C.G. Granqvist, *Appl. Opt.* 20, 2606 (1981).
9. S. Schubert, J. Meiss, L. Müller-Meskamp, and K. Leo, *Adv. Energy Mater.* 3, 438 (2013).
10. H. Jin, C. Tao, M. Velusamy, M. Aljada, Y. Zhang, M. Hambsch, P.L. Burn, and P. Meredith, *Adv. Mater.* 24, 2572 (2012).
11. K. Hong, K. Kim, S. Kim, I. Lee, H. Cho, S. Yoo, H.W. Choi, N.-M. Lee, Y.-H. Tak, and J.L. Lee, *J. Phys. Chem. C* 115, 3453 (2011).
12. P. Dubey, G.A. Lopez, G. Martinez, and C.V. Ramana, *J. Appl. Phys.* 120, 2451031 (2016).
13. P. Chiu, W. Cho, H. Chen, C. Hsiao, and J. Yang, *Nanoscale Res. Lett.* 7, 3041 (2012).
14. D.-T. Nguyen, S. Vedraine, L. Cattin, P. Torchio, M. Morsli, F. Flory, and J.C. Bernède, *J. Appl. Phys.* 112, 635051 (2012).
15. M. Naebe and K. Shirvanimoghaddam, *Appl. Mater. Today* 5, 223 (2016).
16. R.S. Vemuri, M.H. Engelhard, C.V. Ramana, and A.C.S. Appl, *Mater. Interfaces* 4, 1371 (2012).
17. S.M.A. Durrani, E.E. Khawaja, A.M. Al-Shukri, and M.F. Al-Kuhaili, *Energy Build.* 36, 891 (2004).

18. J. Robertson, *Eur. Phys. J. Appl. Phys.* 28, 265 (2004).
19. V. Dave, P. Dubey, H.O. Gupta, and R. Chandra, *Thin Solid Films* 549, 2 (2013).
20. M.F. Al-Kuhaili, *Opt. Mater.* 27, 383 (2004).
21. C.V. Ramana, M. Vargas, G.A. Lopez, M. Noor-A-Alam, M.J. Hernandez, and E.J. Rubio, *Ceram. Int.* 41, 6187 (2015).
22. Z. Wang, X. Ren, C. Fan, Y.-H. Chang, H. Li, H. Chen, S.-P. Feng, S. Shi, and P.K. Chan, *Adv. Mater. Interfaces* 1, 13001191 (2014).
23. J. Shang, G. Liu, H. Yang, X. Zhu, X. Chen, H. Tan, B. Hu, L. Pan, W. Xue, and R.-W. Li, *Adv. Funct. Mater.* 24, 2110 (2014).
24. E.D. Grimley, T. Schenk, X. Sang, M. Pešić, U. Schroeder, T. Mikolajick, and J. LeBeau, *Adv. Electron Mater.* 2, 16001731 (2016).
25. J. Niinistö, K. Kukli, M. Heikkilä, M. Ritala, and M. Leskelä, *Adv. Eng. Mater.* 11, 223 (2009).
26. M.P. Zach, K.H. Ng, and R.M. Penner, *Science* 290, 2120 (2000).
27. D. Shi, G. Wang, C. Li, X. Shen, and Q. Nie, *Vacuum* 138, 101 (2017).
28. H. Wang, X. Ma, and Y. Hao, *Adv. Mater. Interfaces* 4, 16007091 (2017).
29. T. Cramer, A. Sacchetti, M.T. Lobato, P. Barquinha, V. Fischer, M. Benwadih, J. Bablet, E. Fortunato, R. Martins, and B. Fraboni, *Adv. Electron. Mater.* 2, 15004891 (2016).
30. T. Yokoyama, T.D. Dao, K. Chen, S. Ishii, R.P. Sugavaneshwar, M. Kitajima, and T. Nagao, *Adv. Opt. Mater.* 4, 1987 (2016).
31. I.E. Khodasevych, L. Wang, A. Mitchell, and G. Rosengarten, *Adv. Opt. Mater.* 3, 852 (2015).
32. A.A. Demkov, *Phys. Rev. B* 74, 853101 (2006).
33. M. Ramzan, A.M. Rana, E. Ahmed, A.S. Bhatti, M. Hafeez, A. Ali, and M.Y. Nadeem, *Curr. Appl. Phys.* 14, 1854 (2014).
34. N. Selvakumar, H.C. Barshilia, K.S. Rajam, and A. Biswas, *Sol. Energy Mater. Sol. Cells* 94, 1412 (2010).
35. N. Selvakumar and H.C. Barshilia, *Sol. Energy Mater. Sol. Cells* 98, 1 (2012).
36. P. Dubey, J. Gomez, S. Manandhar, V. Shutthanandan, and C.V. Ramana, *Sol. Energy* 166, 146 (2018).
37. M. Vargas, N.R. Murphy, and C.V. Ramana, *Opt. Mater.* 37, 621 (2014).
38. M. Vargas, N.R. Murphy, and C.V. Ramana, *Appl. Phys. Lett.* 104, 1019071 (2014).
39. B. Aguirre, R.S. Vemuri, D. Zubia, M.H. Engelhard, V. Shutthananadan, K.K. Bharathi, and C.V. Ramana, *Appl. Surf. Sci.* 257, 2197 (2011).
40. C.V. Ramana, K.K. Bharathi, A. Garcia, and A.L. Campbell, *J. Phys. Chem. C* 116, 9955 (2012).
41. C.V. Ramana, V.V. Atuchin, V.G. Kesler, V.A. Kochubey, L.D. Pokrovsky, V. Shutthanandan, U. Becker, and R.C. Ewing, *Appl. Surf. Sci.* 253, 5368 (2007).
42. M.E. Walter and B. Eigenmann, *Mater. Sci. Eng. A* 282, 49 (2000).
43. N. Michael and B. Bhushan, *Engineering* 84, 382 (2007).
44. P.R. Elliott, S.P. Stagon, H. Huang, D.U. Furrer, S.F. Burlatsky, and T.P. Filburn, *Sci. Rep.* 5, 92601 (2015).
45. Z. Burton and B. Bhushan, *Nano Lett.* 5, 1607 (2005).
46. M. Senthilkumar, N.K. Sahoo, S. Thakur, and R.B. Tokas, *Appl. Surf. Sci.* 245, 114 (2005).
47. J. Musil, F. Kunc, H. Zeman, and H. Poláková, *Surf. Coat. Technol.* 154, 304 (2002).
48. Y.C. Jung and B. Bhushan, *ACS Nano* 3, 4155 (2009).